ELSEVIER

Polymer 41 (2000) 2169–2182

polymer

Study of the cold drawing of nylon 6 fiber by in-situ simultaneous small- and wide-angle X-ray scattering techniques

J.M. Samon[a], J.M. Schultz[a,*], B.S. Hsiao[b]

[a]*Department of Chemical Engineering, University of Delaware, 125 Colburn Laboratory, Newark, DE 19716-3110, USA*
[b]*Department of Chemistry, State University of New York at Stony Brook, Stony Brook, NY 11794-3400, USA*

Received 31 December 1998; received in revised form 17 May 1999; accepted 19 May 1999

Abstract

The cold drawing of a nylon 6 fiber has been studied with on-line simultaneous small- and wide-angle X-ray scattering techniques. The equatorial crystallinity index, crystalline orientation, and apparent lateral crystallite size as a function of strain were studied by analysis of the wide-angle patterns. The small-angle patterns were examined with the Guinier analysis and the one-dimensional correlation function method to extract morphological parameters such as fibrillar thickness, long period, and lamellar thickness. Upon drawing, the γ-phase was either directly converted to the α-phase or destroyed while amorphous chains were formed into the α-phase due to the increased strain. As strain increased the long period and amorphous thickness increased while the crystalline thickness increased slightly and then leveled off. The shish–kebob morphology, which was seen initially, transformed into a lamellar morphology by the end of the examined drawing process.
© 1999 Elsevier Science Ltd. All rights reserved.

Keywords: Nylon 6 fibers; Cold drawing; Simultaneous small-angle and wide-angle X-ray scattering techniques

1. Introduction

Fibers of nylon 6 exist in two distinct crystalline phases upon crystallizing from the melt after the melt spinning process and subsequent conditioning (annealing and drawing). The amounts of the particular phases depend on the conditions imposed during the spinning and conditioning processes. The α-form [1] consists of a fully extended chain structure with hydrogen bonding between anti-parallel chains. The γ-form's [2] unit cell is slightly smaller along the chain axis (*b*-crystallographic axis) as compared to the α-form. This reduction in unit cell parameters is due to a twisting of the nylon 6 chains resulting from hydrogen bonding occurring between the parallel chains. The hydrogen bonding is poorer in the γ-form as compared to the α-form.

After the initial forming of fibers, they can pass into a second processing step known as cold drawing. In this step, the fibers are elongated at room temperature. This has been shown to alter the crystallinity, orientation, and morphology of the nylon 6 fibers. Small- and wide-angle X-ray scattering techniques, SAXS and WAXS, respectively, are ideal analysis techniques to probe these changes (1–1000 Å) in structure.

As noted by other researchers [3–5] during the drawing of nylon 6 fibers there is an apparent transition from γ-phase crystals to α-phase crystals. The exact underlying physics that explains this behavior, however, has eluded researchers to date. There seem to be two schools of thought on the matter. Arimoto[3] suggested that the γ-phase crystals were destroyed during the drawing procedure and then converted into the fiber structure of the α-phase crystal form. Alternatively, Miyasaka and Makishima [4] have shown that the drawing of nylon 6 at room temperature along the chain direction promotes a crystal–crystal transition from the γ-phase to the α-phase. The critical stress for this transition was estimated to be approximately 400 MPa at room temperature. For this transition to occur two conditions must be satisfied: (1) extension of the γ-phase to untwist the chain around the amide group; and (2) translational mobility of the chain to change the stacking in the crystallite. Below this critical stress this transition is only temporary, and after the load is released, near complete recovery of the starting crystal structure is achieved.

Later Miyasaka and Ishikawa [5] studied the effect of temperature and water on this crystal–crystal transition. It was seen that the transition in drawing dry γ-phase fibers at very low temperatures is more effective than the drawing of wet γ-phase fibers. At these low temperatures water in or surrounding the crystalline regions acts as a cohesive agent

* Corresponding author. Tel.: + 302-831-8145; fax: + 302-831-1048.

0032-3861/00/$ - see front matter © 1999 Elsevier Science Ltd. All rights reserved.
PII: S0032-3861(99)00378-X

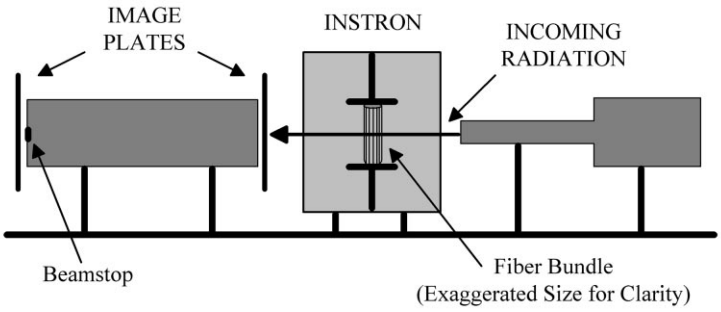

Fig. 1. In-situ SAXS/WAXS cold drawing apparatus.

for the chains and increases the activation energy for the transition. In contrast, stretching in the wet state is more effective for the transition at higher temperatures. An inversion of the effect of water on the transition was seen at about − 60°C. These results are evidence that the transition produced during stretching is a crystal–crystal transition.

More recently Matyi and Crist [6] and Murthy and coworkers [7–9] have used SAXS and/or WAXS techniques to probe drawn nylon 6 fibers more closely. Matyi and Crist [6] used SAXS to conclude that plastic deformation of nylon 6 fibers does not drastically alter the basic two-phase nature of nylon 6. It was also shown that at a large draw ratio, there was evidence for the formation of interfibrillar material. Murthy and coworkers [7–9] used SAXS and WAXS to conclude that nylon 6 has a fibrillar morphology and that the α to γ crystal transition possibly occurs through a metastable crystalline phase. However, in their studies, the fibers used have been previously extended, then the load was released before X-ray analysis. This does not give direct insight into the structural changes occurring during the drawing process because of the possible reversible transition discussed above. Also, there is near total elastic recovery in nylon 6 fibers upon strain release [10] due to the rubbery amorphous phase that exists between the stiffer crystalline lamellae.

Other recent work on the cold drawing of polyethylene [11–13] has eliminated this very problem by examining the material while still in the extended state. In this work [12,13], time-resolved SAXS and WAXS synchrotron techniques are used in conjunction with an in-situ drawing experiment. This allows direct correlation between microscopic and macroscopic deformation measurements. These in-situ measurements during deformation are facilitated by the greater intensity of the synchrotron source as compared to a conventional laboratory source.

In the present work, real time X-ray scattering techniques were conducted on nylon 6 fibers while in the process of being uniaxially drawn in the chain direction. The goal of this work is to compare results of the previous studies on nylon 6 [1–9] with those of an in-situ deformation experiment. This will elucidate the underlying relationship between strain and microscopic and macroscopic structural changes during the cold drawing process. Models of the structural changes during drawing can be constructed from these relationships, gaining a greater understanding of the cold-drawing process with the help of modern experimental and data analysis techniques.

2. Experimental

2.1. Materials and sample preparation

Nylon 6 fibers, which were spun at various take-up speeds (50–300 mpm), were used in this study. The melt spinning procedure to produce these fibers is covered in a previous paper [14]. To maximize the scattering volume for each experiment, a number of fibers (10–30 monofilaments) were aligned parallel to each other during mounting to achieve a sample width normal to the X-ray beam larger than the beam's width. The ends of these fibers were secured to small pieces of aluminum with epoxy, and in turn, these mounted fibers were placed into the grips of a model 4442 Instron tensile testing apparatus. Care was taken in mounting so as not to intertwine the fibers. For all cases the initial gauge length of the samples was 50 mm. The Instron apparatus was mounted so that the fiber was in the beampath, as shown in Fig. 1. Preliminary testing suggested that mounting the fibers as stated above improved the hold of the fibers in the Instron grips and prevented slippage of the fibers while in the grips.

2.2. Synchrotron characterization

The simultaneous in-situ small- and wide-angle X-ray scattering measurements were performed on beamline X3A2 at the National Synchrotron Light Source (NSLS) at Brookhaven National Laboratory in Upton, NY. The synchrotron radiation was monochromatized to 1.28 Å by Bragg reflection from a double silicon (111) crystal monochromator, and was focused and collimated with a gold-coated doubly focusing bent toroidal quartz mirror and a pinhole collimation system. The primary beam intensity was monitored with an ionization chamber.

Two-dimensional SAXS and WAXS patterns were recorded on Fuji HR-V™ image plates (200 × 250 mm)

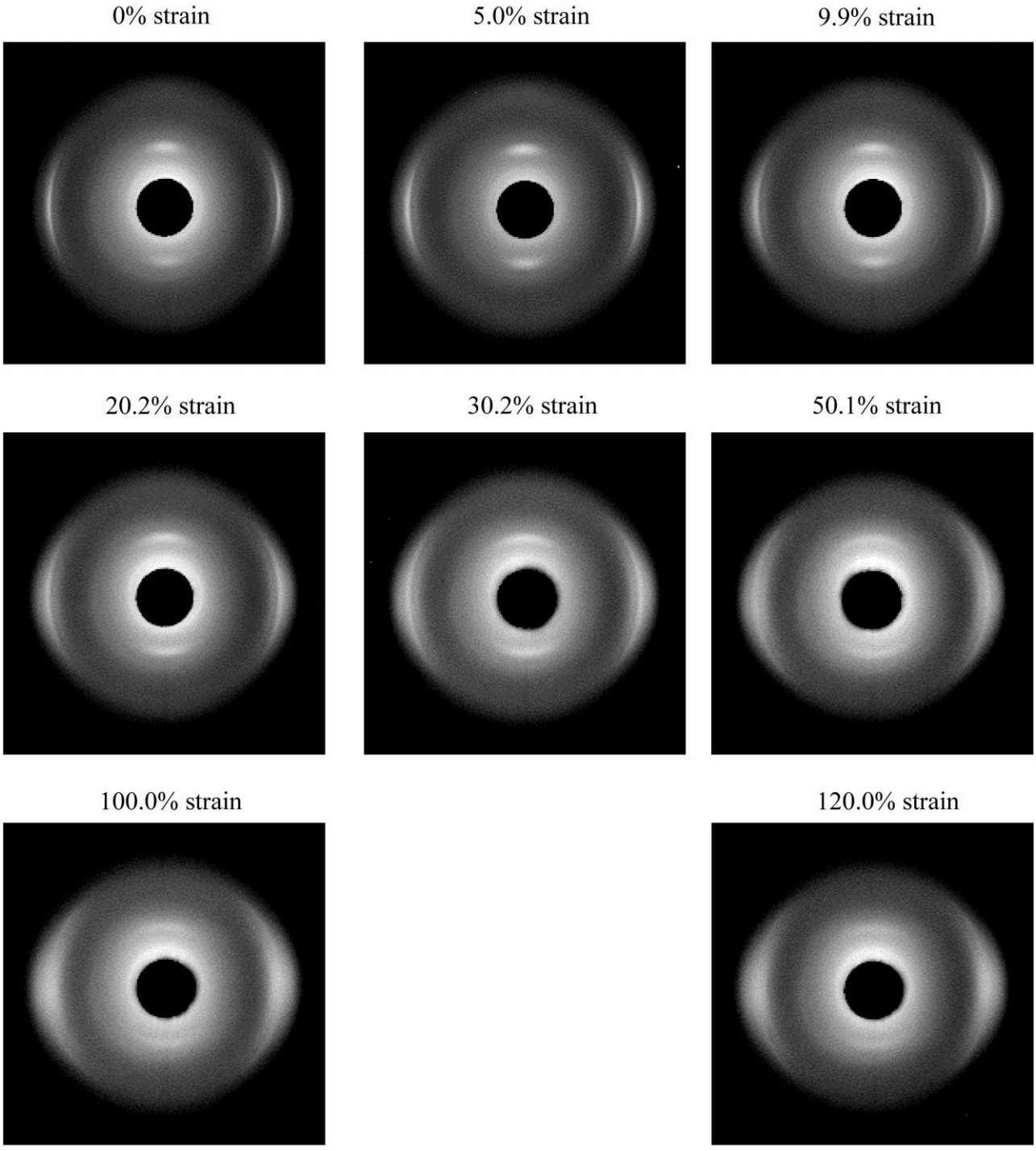

Fig. 2. Two-dimensional WAXS patterns of fibers spun at 300 mpm at the various strain levels as indicated. (Fiber axis vertical.)

with sample-to-detector distances of 1.15 m and 13.1 cm, respectively. The WAXS image plate contains a central hole with a diameter of 2 cm, allowing the passage of the SAXS signal. A Fuji BAS 2000 IP™ image plate scanning station digitized the image recorded on the plates. The SAXS patterns were digitized at a resolution of 200 μm/pixel, while the WAXS patterns had a resolution of 100 μm/pixel.

2.3. Experimental procedure

After the fibers were mounted and placed into the Instron grips, simultaneous SAXS and WAXS images were recorded at collection times ranging from 60 to 120 s, compensating for decreasing intensity of the main beam and the decrease of scattered intensity due to a decrease of the scattering volume. After patterns were recorded at a

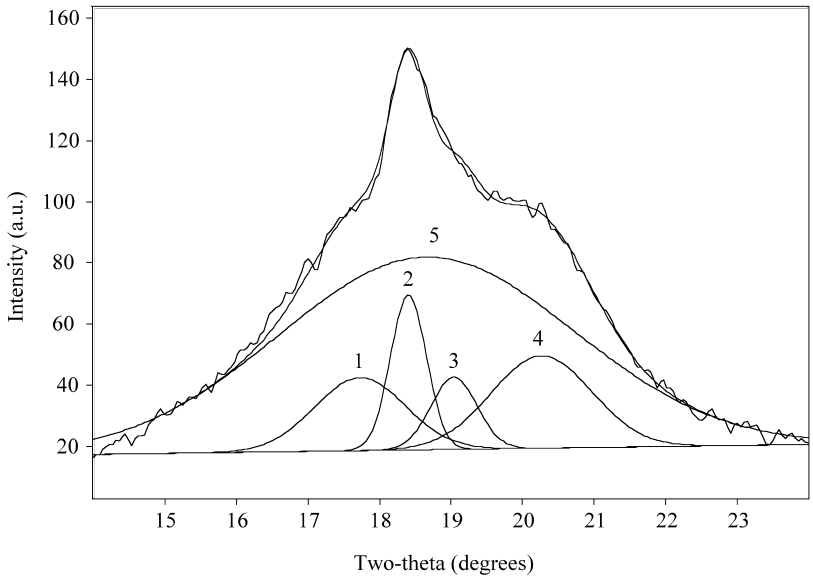

Fig. 3. Deconvolution of an equatorial slice through a two-dimensional WAXS pattern (300 mpm, 0% strain). The peak assignments are: (1) α200; (2) γ001; (3) γ200; (4) α002/202; and (5) amorphous.

strain percentage of zero, the extension was increased at a crosshead speed of 20 mm/min to the next desired extension level, and the next set of patterns was collected after waiting for 10 min. This lag time was to allow the extended fibers to relax to their equilibrium load at the given strain. This procedure was repeated for each extension and each set of fibers.

The scattering patterns were corrected for decay of the primary beam over time and varying collection times. Also, SAXS and WAXS patterns of the system without a fiber sample were subtracted from the fiber patterns to correct for air and instrumental scattering. The effects of sample absorption were neglected due to the small diameter of the fibers studied. The maximum absorption correction using the diameter of the fibers spun at 50 mpm is less than a 10% reduction in intensity. In addition, as strain is increased the diameter of the fibers, and thus the effects of absorption, would decrease as well.

2.4. Data analysis techniques

2.4.1. WAXS

The two-dimensional WAXS images seen during this experiment consisted of five crystalline peaks and one amorphous peak of varying intensities as illustrated in Fig. 2. One crystalline peak appears on the meridian and is a result of the scattering of the γ020 crystal plane. The remaining four crystalline peaks lie on the equator. With increasing values of 2θ(the four crystalline peaks can be assigned to the α200, γ001, γ200, and α002/202 crystal planes. A deconvolution of a typical equatorial slice through a two-dimensional pattern is shown in Fig. 3. The angular range of the collected WAXS patterns was between 5 and 36° in units of 2θ. Due to the strong overlap of the five fitted peaks a small uncertainty in the fitted peak parameters is introduced, and therefore leads to small errors when using these parameters for analysis purposes, such as the equatorial crystallinity index (ECI) discussed below.

The ECI of the fibers was determined by extracting a slice through the equator of the corrected two-dimensional WAXS patterns, and plotting the result as the intensity versus scattering angle. Due to the strong overlap of crystalline and amorphous peak positions, this equatorial slice was used in place of an azimuthal integration. A curve-fitting computer package was then used to fit the experimental data. Since there is substantial overlap between the positions of the amorphous and crystalline peaks, it is helpful to reduce the number of independent variables in the curve-fitting process. Therefore, based on the results of past work [14] the center position of the amorphous peak was fixed to a specific value. The height and full width at half maximum (FWHM) of the amorphous peak was then adjusted so that the tails of the amorphous peak fit the tails of the experimental data. Then Gaussian functions were inserted to fit the crystalline reflections, and their peak parameters (position, height, FWHM) were iterated to achieve a good fit with the experimental data.

After fitting the pattern with an amorphous peak and several crystalline peaks the ECI, was determined as follows:

$$\mathrm{ECI} = \frac{\sum A_{\mathrm{C}}}{\sum (A_{\mathrm{C}} + A_{\mathrm{A}})}, \tag{1}$$

where A_{C} is the integrated area underneath the crystalline peaks and A_{A} is the integrated area of the amorphous peak of the one-dimensional slice. This ECI can be used to compare samples within this experiment for

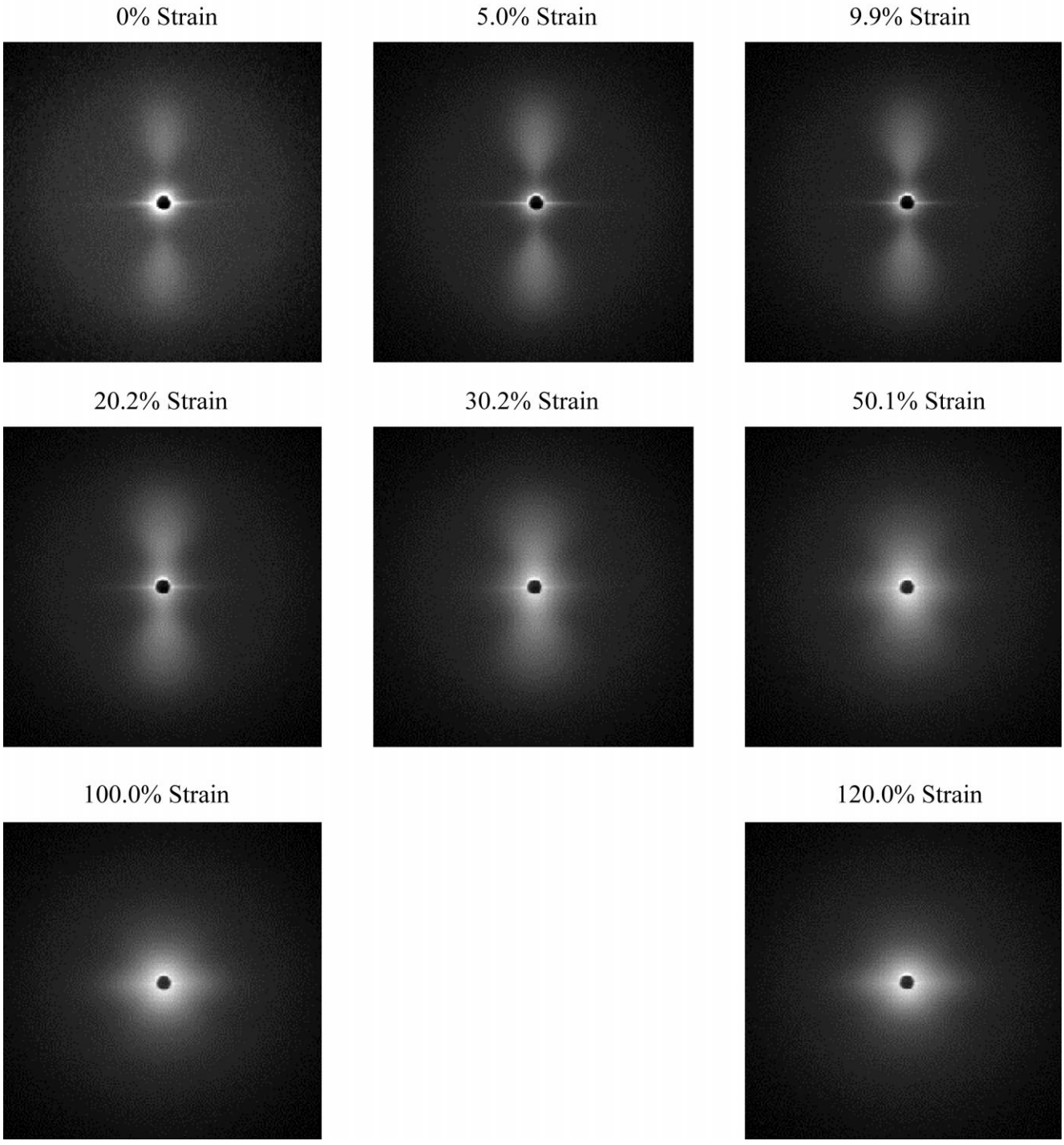

Fig. 4. Two-dimensional SAXS patterns of fibers spun at 300 mpm at the various strain levels as indicated. (Fiber axis vertical.)

qualitative trends, but should not be considered the absolute crystallinity of the sample. It is also noted that the ECI's value can be affected by changes in crystalline orientation. Since the ECI measures only the scattering intensity along the equator, an increase of crystalline orientation might cause the ECI to rise while the true crystallinity remains constant. Nevertheless, if the crystalline orientation is increasing or remains constant while the ECI decreases, the orientation effects do not cloud the qualitative results.

The equatorial slices were also used to find the apparent crystallite size (ACS) using the Sherrer equation [15]

$$\mathrm{ACS} = \frac{0.9\lambda}{(\Delta 2\theta)\cos\theta}, \tag{2}$$

where λ is the X-ray wavelength, $(\Delta 2\theta)$ is the FWHM of the

crystalline peak in radians, θ is half the value of the 2θ position of the center of the crystalline peak.

The crystalline orientation of the fibers was determined quantitatively by computation of the Hermans orientation factor [16] as generalized to a set of three crystallographic axes by Stein [17]. This factor is defined as

$$f_x = \frac{3\langle\cos^2\phi\rangle - 1}{2} \tag{3}$$

where $\langle\cos^2\phi\rangle$ is the averaged value of the square of the cosine of the angle ϕ between the reference direction in the sample (fiber axis) and the x-crystallographic axis. Assuming rotational symmetry about the fiber axis,

$$\langle\cos^2\phi\rangle = \frac{\int_0^{\pi/2} I(\phi)\cos^2\phi\sin\phi\,\mathrm{d}\phi}{\int_0^{\pi/2} I(\phi)\sin\phi\,\mathrm{d}\phi}, \tag{4}$$

where $I(\phi)$ is the intensity diffracted from the (hkl) planes which are normal to the x-crystallographic direction. Therefore f_x values can range from -0.5, when the chains are perpendicular to the x-crystallographic axis, to 1.0, when the chains are parallel to the x-crystallographic axis. When f_x equals zero there is random orientation in the sample.

2.4.2. SAXS

The two-dimensional SAXS patterns seen during this experiment consist of two main features. The first is a pair of broad reflections lying on the meridian. These reflections move inward toward the beamstop with increasing strain. The second is a narrow equatorial streak that grows in intensity and broadens with increasing strain percentage. Fig. 4 shows the various SAXS patterns over a range of strains. The angular range examined in the SAXS patterns ranges from 0.23 to 4.2° in 2θ, which translates to a q range from 0.02 to 0.36 Å^{-1}. Where q, the scattering vector, is defined as

$$q = \frac{4\pi}{\lambda}\sin\theta, \tag{5}$$

where λ is the X-ray wavelength, θ is one half the scattering angle (2θ). The position q_m of the meridional maximum is related by Bragg's law to the long period L_B.

$$q_m = \frac{2\pi}{L_B}. \tag{6}$$

The experimental pattern seen is consistent with a shish–kebob structure, as described by Keller and Kolnaar [18]. This type of morphology is comprised of the shish, which is to be identified with extended chains crystallized into the gamma form, and the kebobs, identified with a lamellar structure of the alpha phase. The formation and development of this morphological structure during the melt spinning of nylon 6 is shown in a previous paper by the authors [14]. The shish structure very quickly forms first under the stress of spinning into imperfect extended chain crystals and upon conditioning at room temperature transforms into the gamma form. The gamma crystal phase, with its less efficient parallel chain alignment, can more easily be formed from extended chain crystals that form during the rapid cooling in the spinline during fiber formation. After the stress is relaxed, the alpha phase with its antiparallel chain arrangement forms kebobs of chain folded crystals around the gamma phase kebobs. The broad meridional peaks in the pattern are consistent with what is seen for a lamellar morphology in a partially oriented system. These lamellae consist of alternating stacks of crystalline and amorphous polymers occurring in a regular arrangement. These alternating stacks are found within the shish structures, as well as, between adjacent kebobs.

To examine the interlamellar structure the one-dimensional correlation function method was used, as proposed by Strobl and Schneider [19]. In the one-dimensional correlation function analysis it is assumed that the lamellar stacks are infinite in height and are perfectly oriented. The scattering from such a theoretical stacking would be a pair of discrete peaks along the stacking direction. In actuality, this scattering due to the lamellae is broadened azimuthally due to the stacks not being exactly parallel to each other. Therefore, the scattering does not appear as a discrete spot, but rather is spread over a section of the reflecting sphere in reciprocal space whose area is proportional to q^2. A Lorentz correction is conventionally used to correct to the value that would be seen for the perfectly oriented case. Ruland [20] has shown that in any partially oriented system a 1D meridional intensity distribution can be analyzed in a similar fashion as that in an isotropic system. That is to say that a Lorentz correction must be used. The only exceptions to this are if the system is completely oriented or the intensity distribution reflects an integrated intensity of the entire SAXS pattern. In the present experiment, the system is partially oriented and it is assumed that the very narrow meridional extraction does not reflect the total integrated intensity of the 2D SAXS pattern.

A 1D meridional slice is taken through the SAXS pattern and a plot of the intensity versus the scattering vector is constructed. The intensity data now is Lorentz-corrected by multiplying the observed intensity by q^2 and plotting the result as a function of q. The correlation function is calculated as

$$\gamma(r) = \frac{\int_0^{\infty} I_{cor}(q)\cos(qr)\,\mathrm{d}q}{Q}, \tag{7}$$

where I_{cor} is the Lorentz-corrected intensity and Q is the invariant, which is defined as

$$Q = \int_0^{\infty} I_{cor}(q)\,\mathrm{d}q, \tag{8}$$

In Eqs. (7) and (8) above, the integration on q as stated should be carried out between zero and infinity. Since this range is too large to be covered experimentally, the

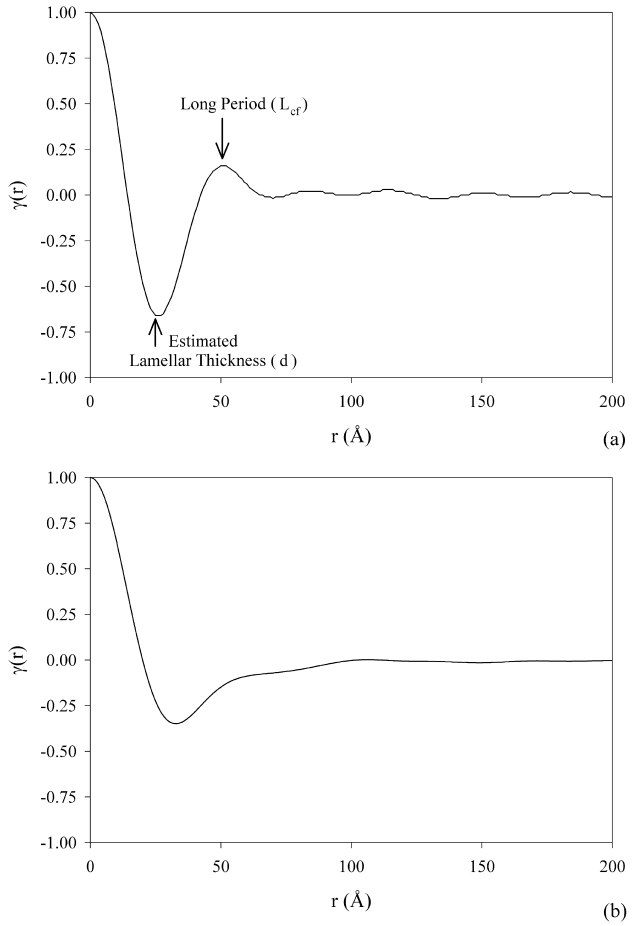

Fig. 5. Typical one-dimensional correlation functions as illustrated by fibers spun at 300 mpm and extended to 15% strain. The positions of the estimated lamellar thickness (d) and the long period (L_{cf}) are indicated above. (a) Using a Lorentz correction; (b) not using a Lorentz correction.

integration can be divided into three different regions. For example, Eq. (8) can be rewritten as [21]

$$Q = \int_0^{q_1} I_{cor}(q)\,dq + \int_{q_1}^{q_p} I_{cor}(q)\,dq + \int_{q_p}^{\infty} I_{cor}(q)\,dq, \qquad (9)$$

where the detector minimum and maximum q values are q_1 and q_2, respectively. The corrected intensity data for the first integral can be found by extrapolating the corrected experimental data back from q_1 to zero. The intensity for the second integral is the corrected intensity calculated from the observed data. The third integral's integrand is calculated by Porod's law with q_p being the beginning of the Porod region ($q_p < q_2$). In the Porod region the intensity decays as the scattering vector to the fourth power. For the present study's experimental data there is a point where the experimental scattered intensity vanishes into the background at a scattering vector which is less than q_2. For this case, as prompted by another work [6], the third integral is neglected.

The correlation function, $\gamma(r)$, is a measure of the electron density in the lamellar stacks, and a typical correlation function is shown in Fig. 5 for both the Lorentz and non-Lorentz corrected data as a comparison. The reason for choosing a Lorentz correction is threefold. First as stated above, the theory of Ruland suggests that in these types of partially oriented systems the correction is required. Secondly, in the examination of the non-Lorentz corrected correlation function, it is seen that the form of the curve does not match the expected shape as is expressed in the correlation function that is calculated from the Lorentz corrected data. Finally, if it is assumed that the shoulder occurring at approximately 60 Å for the non-corrected plot is the first maximum of the correlation function, both the corrected and non-corrected correlation functions give similar values and trends for the long period and lamellar thickness, as discussed below.

The position of the first peak minimum very closely corresponds with the lamellar thickness (d), while the position of the first peak maximum corresponds with the long period (L_{cf}). The true lamellar thickness should be calculated from the intersection of the extrapolation of lines whose slopes and intercepts are functions of the density of the crystalline and amorphous phases and the total crystallinity of the sample. Due to the difficulty in this extrapolation it is assumed that the first minimum in the correlation function corresponds closely with the true lamellar thickness. It is impossible from this analysis, however, to determine if the lamellar thickness corresponds to the amorphous or crystalline thickness. Other aspects of the data must be analyzed to determine the proper assignment of the lamellar thickness.

The equatorial streak seen in the pattern can arise from a variety of sources. This scattering can be a result of voids, individual fibrils or aggregates of fibrils, or reflection from the fiber surface. The possibility that this scattering is a result of scattering from voids or reflection from the fiber surface can be eliminated from examining the intensity of the meridional and equatorial scattering. If either one of these sources were valid, the equatorial scattering would be orders of magnitude greater than the meridional scattering. This is not the case and the meridional and equatorial scattering is of the same magnitude. With this in mind, the most likely source of the equatorial streak is scattering arising from individual shish structures, which are aligned with the fiber axis. In analyzing this streak, a Guinier plot was constructed by plotting the natural logarithm of the equatorial intensity after all background corrections versus the square of the scattering vector. The intensity at small q values in the Guinier plot is related to the radius of individual rod-like scatterers by the following equation [22]:

$$I(q) = K \exp\left(\frac{-q^2R^2}{4}\right), \qquad (10)$$

where q is the scattering vector, R is the radius of the

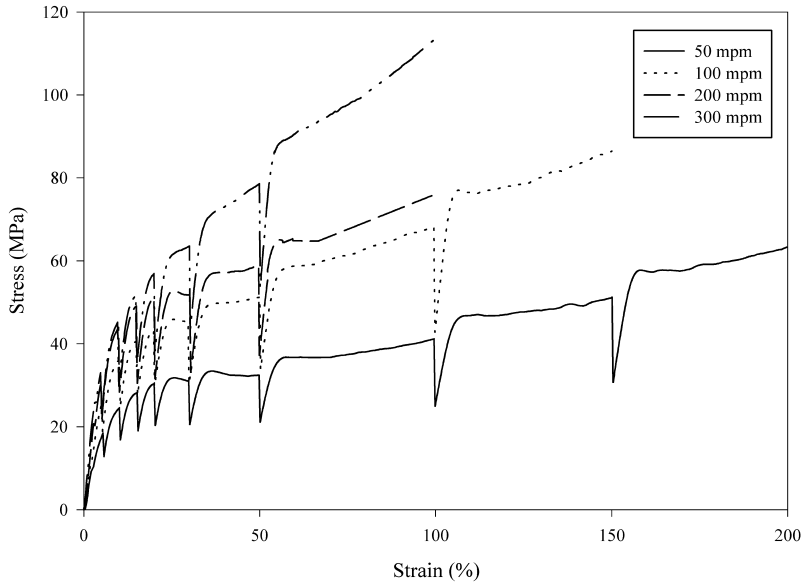

Fig. 6. Stress–strain curves for the various nylon 6 fibers used in this study. Scattering patterns were recorded at each of the sharp troughs.

scattering cylinders in a direction normal to the incident X-ray beam, and K is a constant. Although the theory on which this Guinier analysis is based was derived from a low concentration assumption, the theory can be extended to the case of a more concentrated system so long as the particles are not similar in shape [23].

3. Results and discussion

3.1. Mechanical testing

Fig. 6 shows the stress–strain curves for the various fibers used in this study. X-ray scattering patterns were taken at each of the sharp troughs in the stress–strain curve. At these points the stress had decreased to its near equilibrium value at that specific strain level. At a specific strain percentage, the fibers spun at higher take-up speeds possess higher stress levels. For all take-up speeds at strain levels of approximately 20% and greater, strain hardening is apparent from the near linear rise of stress with increasing strain after the plastic deformation regions. The strain was homogeneous for all take-up speeds examined. Evidence against necking includes direct observation of the fiber during deformation, the observation that fiber failure occurs near the grips, as opposed to in the center of the sample, and physical examination of the fibers after failure. Also, in examination of Fig. 6 there seems to be no point at which an increase of strain is accompanied by a constant stress (an indication of necking).

3.2. WAXS

Fig. 2 again shows wide-angle X-ray scattering patterns at various extensions during the drawing process for fibers spun at a take-up speed of 300 mpm. These patterns' features are representative of fibers spun at all take-up speeds examined. From initial examination of these patterns it is seen that the meridional γ020 peak fades away slowly and by the final strain of 120% it has all but disappeared. Also by inspection, the overall crystalline scattering seems to decrease as strain is increased.

3.3. Equatorial crystallinity index

The γ-phase, α-phase, and total (α + γ) ECIs are shown in Fig. 7 as calculated from Eq. (1). Due to the small uncertainty of the peak fitting discussed above, all ECI values have an experimental range, which is indicated on the figure as error bars. For these error bar curve-fits the heights of all crystalline and amorphous peaks were free to vary while systematically varying the height of the amorphous peak, during which time the FWHM and centroid positions of all the peaks were held constant. These error bars were calculated from fits of the experimental data with χ^2 values 10% greater than the minimum χ^2 value that was used to determine the data points.

The γ-phase ECI decreases for all take-up speeds as the strain percentage increases. Also for all take-up speeds, after 100% strain no residual γ-phase crystallinity can be observed in the equatorial scans although there is perhaps some residual γ-phase due to the existence of a very faint γ020 peak. At strains less than 100% the magnitude of the γ-phase ECI is higher for the lower take-up speeds at a given strain level. The α-phase crystallinity increases sharply from its initial value at 0% strain to a maximum occurring at approximately 20% strain, after which the equatorial crystallinity decreases to an asymptotic value by 100% strain. These trends are seen for all take-up speeds. The magnitude of the α-phase ECI again shows the same relationship with the take-up speed, as stated above, at a

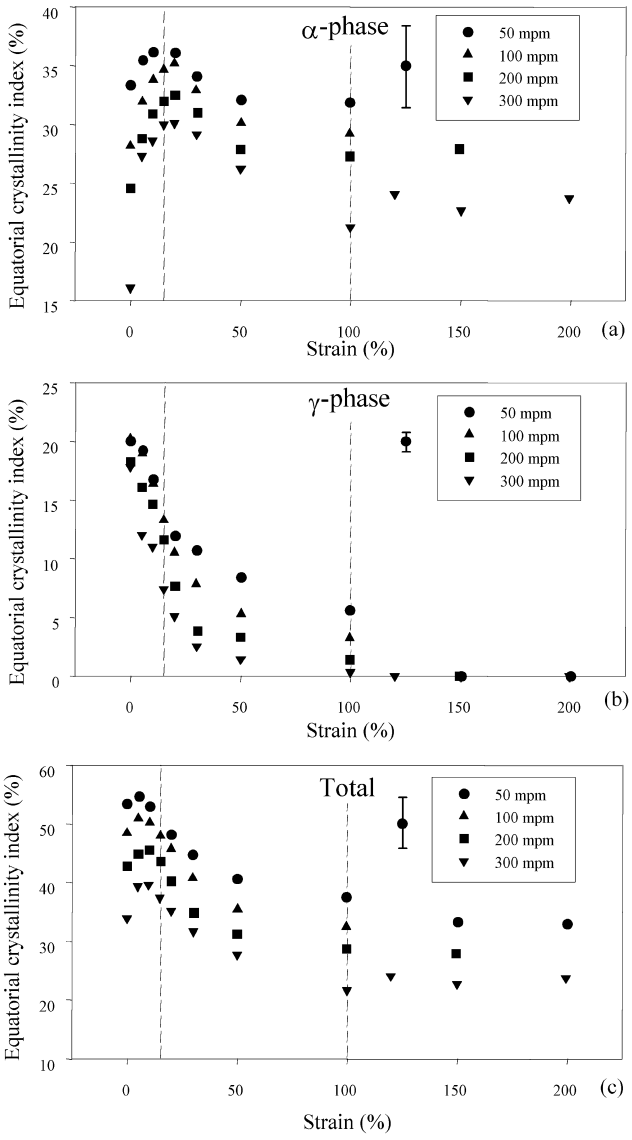

Fig. 7. The equatorial crystallinity index as a function of take-up speed and strain percentage of the: (a) α-phase; (b) γ-phase; and (c) total (α + γ).

particular strain. The total (α + γ) ECI increases from its initial value at zero strain to a maximum at about 10% strain. From this point the total ECI decreases to a limiting value of 100%, slowly. The total ECI also follows the above-stated relationship with take-up speed. By analysis of a meridional integration of the corrected 2D WAXS pattern (not shown), the area under the γ020 peak decreases monotonically during the drawing process. The decrease in area under the γ020 peak further supports that the γ-phase is in fact disappearing with increasing strain percentage even if the crystalline orientation is decreasing. This integration was carried out over the γ020 peak in two-dimensions rather than only over a meridional slice; therefore all orientation effects were taken into account.

The universal dependence of the magnitude of the γ-phase, α-phase, and total ECI on take-up speed is a result of the previous history of the fibers. Fibers spun at lower take-up speeds have longer amounts of time for crystallization to occur during the melt spinning process; therefore they exhibit higher degrees of crystallinity. This property dominates the changes due to the strain on the specimen, so that at all strain percentages the lower take-up speeds always have the highest degree of ECI and vice versa.

The dependence of the ECI on strain percentage is slightly more complicated. It is appropriate to break the strain percentages into three distinct regimes: regime I (0–15% strain); regime II (15–100% strain); and regime III (100% strain and greater). Dashed lines in Fig. 6 indicate the regime boundaries. In regime I the gamma ECI decreases while both the alpha and total ECI increase. The majority of this increase occurs after the first extension, from 0 to 5% strain. The increase of the alpha ECI is always greater in magnitude than the decrease of the gamma ECI in this region; so the net result, the total ECI, is increasing as well. In the second regime the α-phase, γ-phase, and total ECI are all decreasing. Finally, in the third regime the α-phase ECI remains constant and the γ-phase ECI has dropped to zero, thus forcing the total ECI to remain constant as well.

The increase in the α-phase ECI could be due to three possible phenomena, which may occur simultaneously. The α-phase ECI might be raised: (1) by conversion of the γ-phase to the α-phase in a crystal–crystal transition; (2) by conversion of the amorphous phase to the α-phase; and/or (3) by an increase in the crystalline orientation of the α-phase. It has been shown by Murthy and coworkers [8] that the crystalline orientation of the α- and γ-phases increases with increasing strain. If the crystalline orientation was the only factor affecting the various ECIs, an increase in orientation would result in an increase of the ECI. This is not the case because the γ-phase ECI decreases throughout the straining process. Therefore, the α- and γ-phase ECIs are also being affected by reasons (1) and (2) listed above with minimal influence of the crystalline orientation increase.

Since the increase of the α-phase ECI is greater than the decrease of the γ-phase ECI, a significant percentage of the α-phase increase must be due to conversion of the amorphous phase as opposed to the γ to α conversion. The decrease in the γ-phase ECI could be a result of two competing effects. Either the γ-phase is being converted to the α-phase, as discussed above, or the γ-phase crystals are being destroyed during the drawing process. The γ-phase is more likely to be destroyed outright due to its weaker hydrogen bonds, as compared to the α-phase. It is difficult to distinguish whether the γ-phase is being destroyed and the α-phase is being formed from converted amorphous polymer, or the γ-phase is being converted directly into the α-phase. It can be stated, however, that to some degree the amorphous phase is being transformed to α-phase crystals. Whether this amorphous polymer is a result of γ-phase crystal destruction cannot be substantiated.

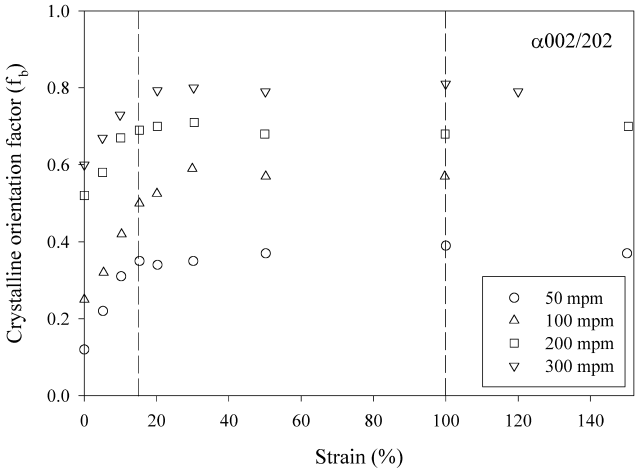

Fig. 8. The Hermans crystalline orientation function of the α002/202 reflection as a function of take-up speed and strain percentage.

3.4. Crystalline orientation

Fig. 8 shows the crystalline orientation of the α002/202 crystalline reflection as a function of take-up speed and strain. As seen in Fig. 3, the α002/202 reflection is the only crystalline reflection that is minimally interfered with by peak overlap at its centroid position. Since all the crystalline scattering at its centroid position is from the α002/202 peak, orientation analysis can be performed with confidence of no peak overlap effects. The crystalline orientation at a given strain level for fibers spun at higher take-up speeds is greater than that of the fibers spun at lower take-up speeds. This is due to the higher take-up speed imparting a larger stress on the fiber as it is being formed, giving rise to an increase in crystalline orientation. More interestingly in examining the effect of the strain percentage on the crystalline orientation, it is seen that the orientation increases from its initial value to a maximum value that occurs at approximately 20–30% strain. At that point the crystalline orientation remains constant. While comparing these results to the results seen in the stress–strain curves of Fig. 6 we see that this leveling off of the crystalline orientation is occurring precisely at the onset of strain hardening.

3.5. Apparent crystallite size

Fig. 9 shows the (ACS) of the γ001 and γ200 peaks as examined by equatorial scans. The size of the γ001 crystallites decreases with strain for all take-up speeds. Lower take-up speeds seem to produce small crystals, while higher take-up speeds produce larger crystals. The size of the crystals of the γ-phase normal to (100) exhibits qualitatively the same variation with take-up speed as the crystal size normal to (001). Their size, however, is not dependent on strain. At strains of 25% and greater the γ200 crystalline peak is not apparent in the equatorial slice. This indicates that the crystals, which grow along this direction, are destroyed at strains greater than 25%.

The α200 and α002/202 crystallite sizes decrease with increasing strain, as shown in Fig. 10. There is no obvious trend in the dependence of α-phase crystallite size on take-up speed in either case. This is not an expected result and may stem from the fact that the crystalline peaks for the alpha reflections are very broad as compared to the gamma reflections. There is a larger percent error in fitting the width of the alpha reflections, and this increased error directly effects the crystallite size calculation.

The fact that the α200, α002/202, and γ001 crystallite sizes decrease with increasing strain is most likely due to the mechanical destruction of lamellar crystals by shear, as suggested by Peterlin [24–27] and depicted by Schultz [28]. The constant crystallite size of the γ200 crystallites at low strains is most likely an effect of the strength of the hydrogen bonding. In the γ-phase of nylon 6, the 200 direction is in the direction of the hydrogen bonding which is perpendicular to the fiber direction. These relatively strong bonds would need to be broken in order to reduce the crystal size along [100], whereas bonds of lower energy are available along [010].

3.6. SAXS

Fig. 4 again shows small-angle X-ray scattering patterns at various extensions during the drawing process for fibers spun at a take-up speed of 300 mpm. These patterns' features are representative of fibers spun at all take-up speeds examined. From initial examination of these patterns a two-lobe pattern with a sharp equatorial streak is seen initially. Upon an increase in strain, the meridional peak moves inward toward the beamstop and by a strain of 30% it has impinged on the beamstop. The equatorial streak's shape remains unchanged until 30% strain. At this point it broadens, but this can be attributed to an increase in intensity due to the impinging meridional peak.

This type of pattern is consistent with a shish–kebob type of microstructure. This microstructure consists of long stacks of kebobs (lamellar crystals) that are built from alternating crystalline and amorphous lamellae skewered together by a long fibril crystal. The neighboring shish–kebobs may be separated by amorphous polymers.

3.7. Analysis of lamellar morphology

Fig. 11 shows the long period of the lamellar stacking as calculated by Bragg's law and alternatively as calculated by the first maximum of the one-dimensional correlation function. In either case there seems to be no clear dependence on the fiber's take-up speed. The long period in either case does, however, increase throughout the drawing process. This indicates that the macroscopic strain being imposed on the fiber is also imparting a microscopic strain on the lamellar stacking. Also shown in Fig. 11(a) and (b) are lines representing equal macroscopic (ϵ) and microscopic ($\Delta L/L$)

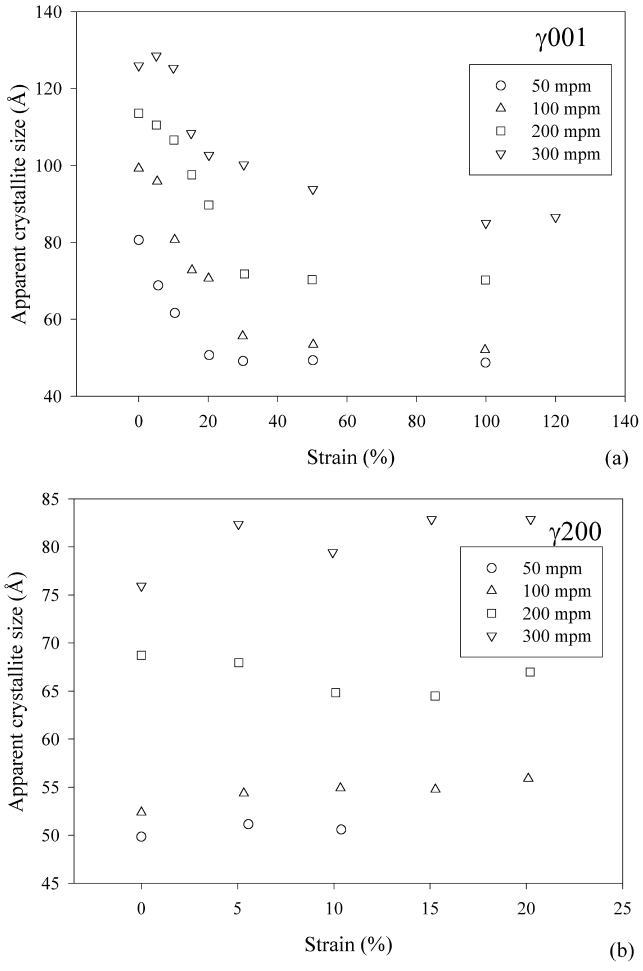

Fig. 9. The apparent size of the: (a) γ001; and (b) γ200 crystallites.

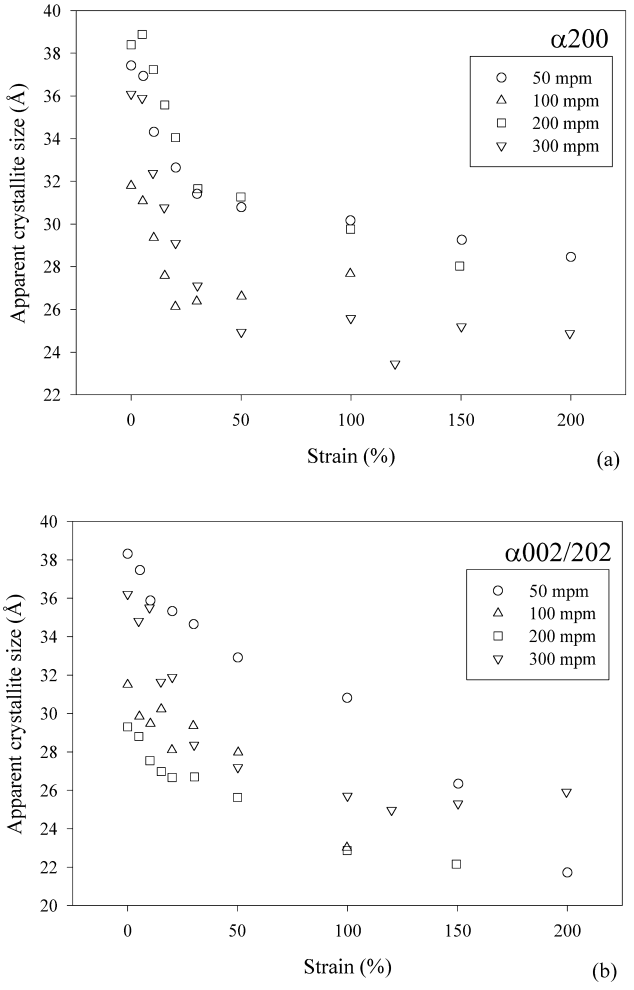

Fig. 10. The apparent size of the: (a) α200; and (b) α002/202 crystallites.

strains. Over the initial deformation (up to 20% strain), the deformation appears to be affine (region I). Thereafter, the rate of increase of $\Delta L/L$ becomes smaller than the macroscopic strain, indicating that the deformation becomes increasingly plastic. It is also to be noted that the long period calculated by Bragg's law is always greater than that calculated by the one-dimensional correlation function analysis. This indicates that the morphology that exists during the drawing of nylon 6 deviates from the ideal two-phase model, as illustrated by Santa Cruz et al. [29] for a PET system.

Fig. 12 shows lamellar thicknesses I and II, respectively, as a function of strain. The former is found by noting the position of the first minimum of the one-dimensional correlation function, while the latter is found by subtraction of lamellar thickness I from the long period as calculated from the correlation function analysis. Lamellar thickness I increases sharply by 20–30% over the first 30% of strain and then remains constant. This final value decreases somewhat with increasing take-up speed. Lamellar thickness II, on the contrary, exhibits a steady increase over the entire macroscopic strain range, to some 2.5 times its original value. No dependence on take-up speed is apparent for either thickness I or II.

The question remains: which lamellar thickness corresponds to the amorphous lamellae and which corresponds to the crystalline lamellae? This question can be answered by combining the results of the correlation function analysis and the ECI analysis. The SAXS linear crystallinity is first calculated by taking the ratio of one lamellar thickness (either I or II) to the total long period as calculated by the correlation function analysis. This ratio's qualitative trends should be in near agreement with the qualitative trends seen in the total ECI values extracted from the WAXS patterns. For example, at strains of 30% and greater, there are only very slight changes in the total ECI, and likewise, there are only slight changes in lamellar thickness I. At this time lamellar thickness II is still growing at a substantial rate. Therefore lamellar thickness I is assigned to the crystalline phase, and lamellar thickness II is assigned to the amorphous phase.

Structurally, the small initial extensions result in microscopic extension of both the crystalline and amorphous layers. At approximately 30% strain the crystalline lamellae's thickness starts to remain constant, while the amorphous layers either continue to be mechanically extended or

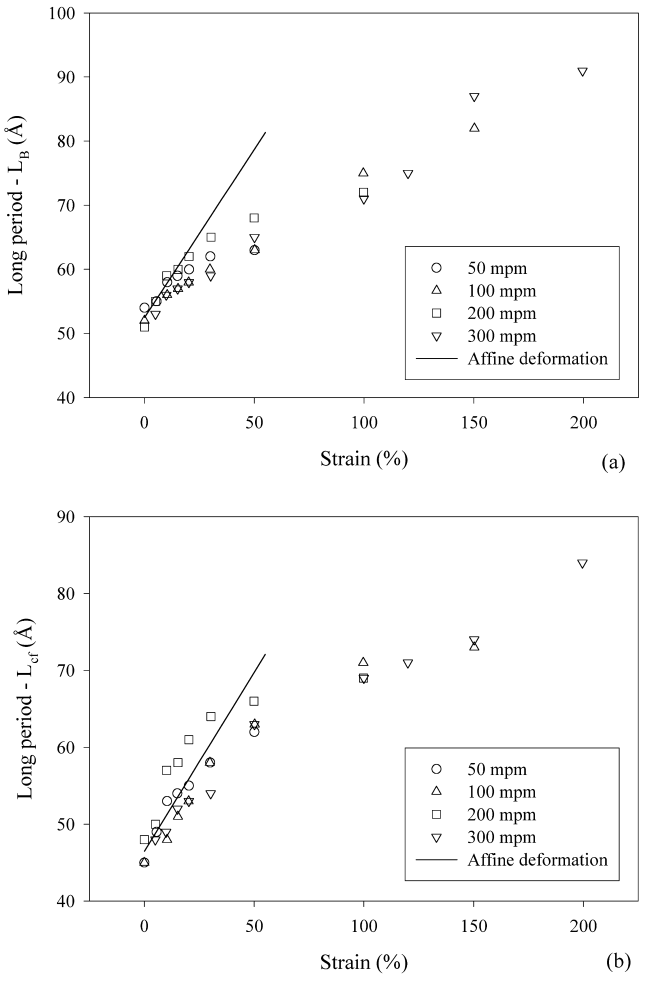

Fig. 11. The long period of the fiber samples as calculated by: (a) Bragg's law; and (b) one-dimensional correlation function analysis. The solid line indicates a perfectly affine deformation based on the average long period at zero strain.

small crystals begin to be destroyed. It is not reasonable that the crystalline material mechanically strains 30%. More likely, the increase in thickness is due to mechanically induced crystallization of material in a transition layer between crystals and more random amorphous packing. This is consistent with the observed initial increase in crystallinity. The prolonged and continuous increase of the amorphous thickness most likely reflects both elastic stretching of chains in the amorphous layer and the conversion of crystalline matter into non-crystalline matter.

3.8. Equatorial streak

The equatorial streak was analyzed by the construction of a Guinier plot, as stated above. For all scattering patterns the plot consisted of two linear regimes, occurring above and below a point corresponding to approximately one half degree two-theta ($q = 0.043$ Å^{-1}). Analysis of the first region provides an approximate dimension of the fibril thickness, as seen in Fig. 13. The second region should be discarded because the Guinier approximation is valid only in the small-angle limit. The fibrillar thickness decreases with increasing strain percentage until 100% strain, where it levels out. At all strains, an increase in take-up speed translates into a decrease in the fibrillar thickness.

These internal microstructural changes in the fibrillar structure of the nylon 6 fiber are interrelated with the external macrostructural strain being imposed on the fiber. On the macrostructural size scale as the fiber is elongated the fiber thickness perpendicular to the draw direction decreases. Along with these macroscopic changes, the thickness of the fibril on a microstructural size scale is also decreasing as seen by the Guinier analysis. The explanation of this phenomenon is complicated by the fact that alpha and gamma crystals are being destroyed and thus the shish–kebob structure is being torn apart.

3.9. Structural model of shish destruction

From the small-angle results it is apparent that the nylon 6

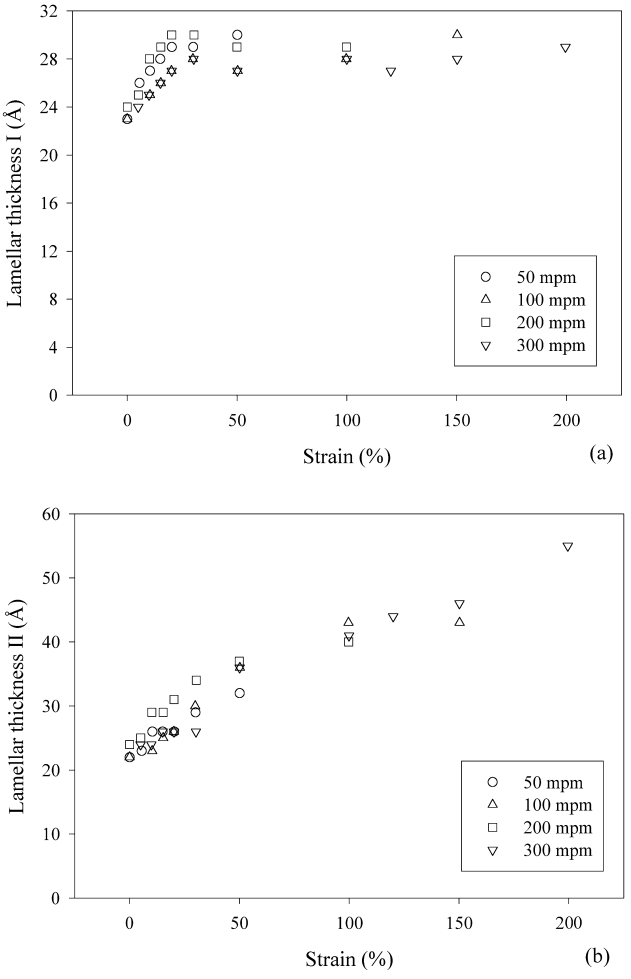

Fig. 12. Lamellar thickness: (a) I; and (b) II as calculated by the one-dimensional correlation function analysis. Lamellar thickness I is assigned as the crystal thickness while lamellar thickness II was determined to be the amorphous thickness.

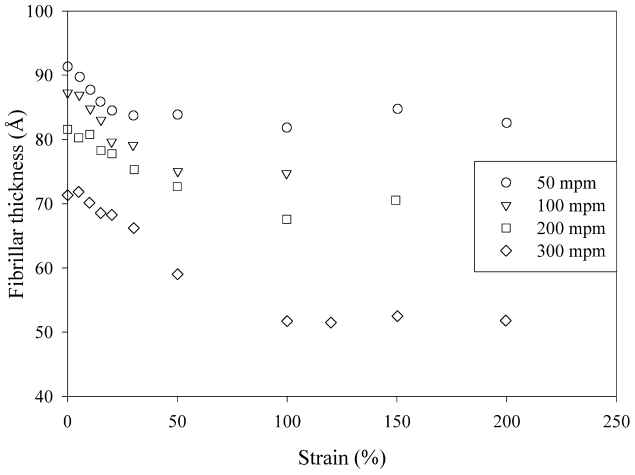

Fig. 13. The fibrillar diameter as a function as take-up speed and strain percentage as calculated from Guinier analysis.

fibers exhibit a shish–kebob type morphology. The shish is composed of both the γ-phase of nylon 6, which forms in the spinning process due to its less organized parallel chain stacking arrangement, and of amorphous polymer. These structures are composed of a lamellar stacking of crystalline and amorphous zones. Regularly spaced along the shish are pockets of α-phase crystals in groupings known as kebobs, which crystallize in an anti-parallel chain-stacking pattern. The kebobs are in a lamellar stacking pattern with additional amorphous phase intervening between the crystalline lamellae. The fraction of so-called shish structures is small as compared to that of the kebobs.

As the nylon 6 fibers are placed under small amounts of strain (< 20%), there is an affine deformation of both the crystalline and amorphous components of the shish–kebob structure. This increases the amorphous and crystalline lamellar spacing as well as the overall long period. From strains of 0–15% (regime I) the shish structures which comprise extended chain γ-phase crystals begin to be torn apart. At this point they are either becoming amorphous polymers or are transforming directly into α-phase crystals. There is also an influence of the increase of crystalline orientation on the α- and γ-phase ECIs, but this effect is thought to be minimal, as discussed above. Amorphous polymers surrounding the shish–kebob structure may be transformed into α-phase crystals, thus increasing both the α-phase and total ECI. It is difficult to say, however, if this newly formed α-phase was formed from amorphous polymers that were once γ-phase crystals or if the γ-phase crystals are undergoing a crystal–crystal transition directly to the α-phase. Towards, the end of this regime the production of the new α-phase slows and the net change in ECI becomes negative. As the strain reaches regime II (15–100% strain) the α-phase crystals begin to be destroyed in addition to the γ-phase shishes. The long period is now increasing mainly due to the destruction of poorly formed α-phase kebobs. This eliminates specific kebobs along the

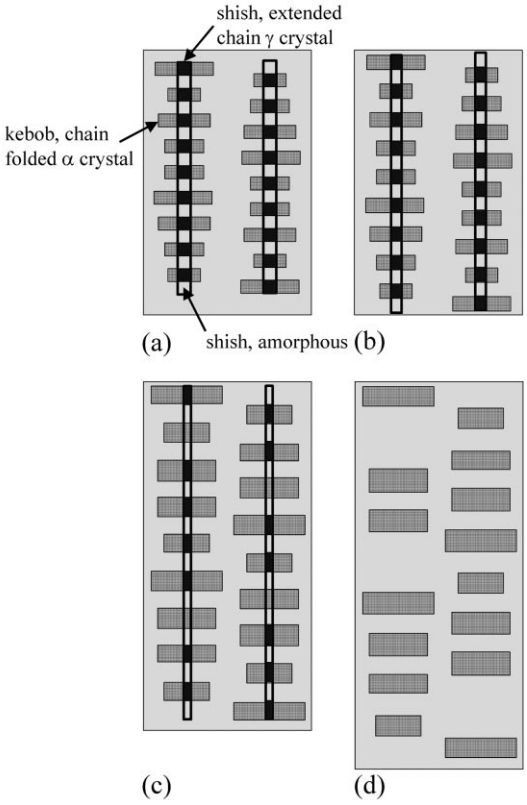

Fig. 14. A possible mechanism of the shish–kebob to lamellar transformation. (a) The initial shish is placed under strain. (b) Under small amounts of strain the crystalline and amorphous segments undergo affine deformation (regime I). (c) Under larger amounts of strain extended chain gamma crystals begin to be transformed into chain folded alpha crystals (regime II). (d) Finally, the extended chain structure is totally destroyed as well as some poorly formed kebobs and a lamellar structure remains (regime III). (The reduction of fibrillar thickness is not shown in the above figure.)

shish. This reduces the periodicity of kebobs along the shish subsequently reducing the discrete scattering from the lamellar stacking along the shish. The distance between the remaining kebobs increases, thus increasing the long period. Finally, in regime III (> 100% strain) most if not all of the extend chain γ-phase shishes have been destroyed or transformed to α-phase crystals and the morphology becomes lamellar with alternating stacks of amorphous and α-phase crystalline polymers. Fig. 14 shows a possible mechanism of the shish–kebob to lamellar transformation pictorially. With increased stress, these lamellar stacks then transform to a microfibrillar type structure probably through the mechanism described by Peterlin [26]. With the now non-regular spacing along the fiber axis only equatorial scattering in produced by these microfibrils.

4. Conclusions

This study uses modern synchrotron X-ray scattering techniques to probe the nylon 6 fiber system while under elongational strain. With these analytical techniques, the

structural and morphological changes that accompany the increase in strain can be probed. This work further clarifies past work by other research groups on the nylon 6-fiber system.

While examining the stress–strain curves for the fibers spun at various take-up speeds, strain hardening is apparent at strains of about 20% and greater. This is the point at which the α-phase crystallinity index reaches its maximum and the crystalline orientation and the crystalline lamellar thickness reach their asymptotic values. Also, by 20–30% strain much of the γ-phase has been either converted or destroyed, eliminating much of the shish from the shish–kebob structure. This study verifies that a part of the observed γ-phase to α-phase conversion results from destruction of the γ-phase and the production of the α-phase from amorphous polymers. Although it is difficult to rule out a crystal–crystal transition entirely, amorphous to α-phase conversion is occurring. Over the course of the cold drawing the shish–kebob morphology transforms into a lamellar morphology, which ultimately transforms into a microfibrillar morphology. A possible mechanism for the shish–kebob to lamellar to microfibrillar transformation is proposed, with an explanation based on examination of the equatorial crystallinity and SAXS results.

Acknowledgements

This work was supported by a grant from the NSF-GOALI program (DMA-9629825).

References

[1] Brill R. Z Physik Chem 1943;B53:61.
[2] Arimoto H, Ishibashi M, Hirai M, Chatani Y. J Polym Sci 1965;A3:317.
[3] Arimoto H. Kobunshi Kagaku 1962;19:212.
[4] Miyasaka K, Makishima K. J Polym Sci Pt A1 1967;5:3017.
[5] Miyasaka K, Ishikawa K. J Polym Sci Pt A2 1968;6:1317.
[6] Matyi RJ, Crist Jr B. J Polym Sci, Polym Phys 1978;16:1329.
[7] Murthy NS. Polym Comm 1991;32:301.
[8] Murthy NS, Bray RG, Correale ST, Moore RAF. Polymer 1995;36:3863.
[9] Murthy NS, Bednarczyk C, Moore RAF, Grubb DT. J Polym Sci, Polym Phys 1996;34:821.
[10] Drexler PG, Tesoro GC. In: Lewin M, Sello SB, editors. Handbook of fiber science and technology: chemical processing of fibers and fabrics, New York: Dekker, 1984. pp. 14 chap. 1.
[11] Kaufman WE, Schultz JM. J Mater Sci 1973;8:41.
[12] Butler MF, Donald AM, Ryan AJ. Polymer 1997;38:5521.
[13] Butler MF, Donald AM, Ryan AJ. Polymer 1998;39:39.
[14] Samon JM, Schultz JM, Wu J, Hsiao BS, Yeh F, Kolb R. J Polym Sci, Polym Phys 1999;37:1277.
[15] Guinier A. X-ray diffraction in crystals, imperfect crystals, and amorphous bodies, San Francisco: Freeman, 1963.
[16] Hermans JJ, Hermans PH, Vermeas D, Weidinger A. Rec Chim Trav 1946;65:427.
[17] Stein RS. J Polym Sci 1958;31:327.
[18] Keller A, Kolnaar HWH. In: Cahn RW, Hassen P, Kramer EJ, editors. Materials science and technology, a comprehensive treatment, 18. VCH, 1997. pp. 190 chap. 4.
[19] Strobl GR, Schneider M. J Polym Sci, Polym Phys 1980;18:1343.
[20] Ruland W. Coll Polym Sci 1978;256:932.
[21] Russell T. In: Brown G, Moncton DE, editors. Handbook on synchrotron radiation, 3. New York: Elsevier, 1991. pp. 379 chap. 11.
[22] Guinier A, Fournet G. Small-angle scattering of X-rays, New York: Wiley, 1955 p. 27.
[23] Guinier A, Fournet G. Small-angle scattering of X-rays, New York: Wiley, 1955 p. 70.
[24] Ingram P, Kiho H, Peterlin A. J Polym Sci 1967;C16:1857.
[25] Peterlin A. Kolloid-ZZ Polymere 1969;233:857.
[26] Peterlin A. J Mater Sci 1971;6:490.
[27] Peterlin A. Coll Polym Sci 1987;265:357.
[28] Schultz JM. Polymer material science, Englewood Cliffs, NJ: Prentice-Hall, 1974 pp. 497–501.
[29] Santa Cruz C, Stribeck N, Zachmann HG, Baltá Calleja FJ. Macromol 1991;24:5980.